ANITA anomalous events and axion quark nuggets

Xunyu Liang and Ariel Zhitnitsky
Department of Physics and Astronomy, University of British Columbia,
Vancouver, V6T 1Z1 British Columbia, Canada

(Received 18 May 2021; accepted 12 September 2022; published 26 September 2022)

The Antarctic Impulse Transient Antenna (ANITA) Collaboration [1–3] has reported two anomalous events with noninverted polarity. These events are hard to explain in terms of conventional cosmic rays (CRs). We explore a new possible explanation for these anomalous events by suggesting that these events can be related to the dark matter (DM) annihilations within the so-called axion quark nugget (AQN) DM model. This model was initially invented for a completely different purpose: to explain the observed similarity between the dark and the visible components in the Universe—i.e., $\Omega_{\mathrm{DM}} \sim \Omega_{\mathrm{visible}}$—without any fitting parameters. We investigate the signal properties of the upward-going AQN events, including the event rate, the pulse duration, and the electric field strength, and find them consistent with the observations. We list several features of the upward-going AQN events distinct from conventional CR air showers. The observations (or nonobservation) of these features may substantiate (or refute) our proposal.

DOI: 10.1103/PhysRevD.106.063022

I. INTRODUCTION

The Antarctic Impulse Transient Antenna (ANITA) Collaboration has observed [1–3] two anomalous events that appear to be energetic cosmic showers emerging from the Earth with large exit angles. We advocate a possible explanation for these ANITA anomalous events (AAEs) in the so-called axion quark nugget (AQN) model [4]. This model was invented long ago with no relation to the ANITA observations. Instead, it was dedicated to explaining the observed similarity between the dark matter (DM) and the visible densities in the Universe—i.e., $\Omega_{\mathrm{DM}} \sim \Omega_{\mathrm{visible}}$—without fine tuning. Nevertheless, we will show that an upward-going AQN event can reproduce consistent signal properties of the AAEs, including the event rate, the pulse duration, and the electric field strength.

The ANITA experiment has completed four flights [1–3] and reported two AAEs that are compatible with a ν_τ neutrino interpretation of energy ~EeV at exit angles of $-27°$ and $-35°$ relative to horizontal in the first [1] and third [2] flights, respectively. The radio pulse of an AAE observed by the ANITA balloon payload at an altitude of ~ 35 km is of the order $(0.1-1)$ mV/m in electric field strength and (1–10) ns in time duration. The observed frequency spectrum of the signal is in the range (40–800) MHz. It attenuates sharply beyond the critical frequency near 800 MHz. Numerous suggestions [5–31] are proposed to explain the AAEs, but many of them suffer from difficulties; see below.

The AAEs are in critical tension with the standard model (SM) because neutrinos are exceedingly unlikely to traverse through Earth at a distance of $\gtrsim 5 \times 10^3$ km with such ultrahigh energy, even accounting for the ν_τ regeneration [1]. The analysis [5] reviewed the high-energy neutrino events from the IceCube Neutrino Observatory and inferred that the ν_τ interpretation is excluded by at least 5σ confidence. A similar study in Ref. [6] estimated ANITA acceptance to a ν_τ flux and concluded at least 2 orders of magnitude above the upper limit from Pierre Auger Observatory and IceCube. More recently, IceCube also published severe constraints of astrophysical explanation for the AAEs under SM assumptions [7].

Alternative explanations such as transition radiation [8,9] remain unconfirmed, special reflection on a spherical surface is disfavored [10], and glaciological explanation based on subsurface reflectors [11] is largely excluded by ANITA [12]. Notably, several beyond-the-SM (BSM) explanations are proposed [13–30]. In most cases, it suggests the origin of a (or a group of) massive hypothetical particle(s), which is strongly constrained by the IceCube and Auger bounds [31]. The other common problem is that the models are largely fine-tuned to match the observation of the AAEs and lack a natural motivation.

The AQN model, as an explanation of the AAEs, does not encounter the above difficulties. The AQN is a macroscopic DM candidate with a mass of grams and a size of 0.1 μm. Hence, an upward-going AQN event is distinct from the conventional CR air showers induced by ultrahigh-energy particles. The constraints from the Pierre Auger Observatory

---

and IceCube are not applicable in the AQN scenario, because numerous basic assumptions of the CR features are invalid.

The *fundamental* parameter of the model, such as the AQN's size R and the average baryon charge $\langle B\rangle$ of the AQNs, is constrained by various phenomena and observations long ago irrelevant to the AAEs. In this sense, the AQN model is rigid and predictive, since there is little flexibility or freedom to modify the fundamental parameters mentioned above. This comment applies to the model itself, not to the interactions with the environment, which could be complex. The description of the interaction with surrounding material requires the introduction of unknown *phenomenological* parameters, which cannot be computed from the first principles.

In the following Sec. II, we present a short overview of the AQN model. In particular, Sec. II A introduces the fundamental facts of the model, and Secs. II B and II C summarize the essential features relevant to the present work. Section III describes the properties of an AQN at the instant when it emerges from the Earth's surface. Sections IV and V examine the signal properties of an upward-going AQN event, including the event rate, the pulse duration, and the electric field strength. We conclude in Sec. VI, where we explicitly formulate some distinct features between upward-going AQN events and conventional CR events. We also suggest possible tests which may support or refute our proposal.

II. THE AQN DM MODEL

We start with a few historical remarks and the motivation of the AQN model in Sec. II A. In Sec. II B, we overview several recent observations possibly related to an AQN hitting the Earth, including the puzzling bursts observed by the Telescope Array experiment, the exotic events recorded by the Pierre Auger observatory, and the multimodal clustering events observed by the HORIZON 10T instrument. In Sec. II C, we review specific characteristics of the AQNs traversing the Earth, such as internal temperature and ionization level. These characteristics will be necessary for interpreting the AAEs as the Earth-emergent AQN events.

A. The basics

The AQN DM model [31] was solely motivated to explain the observed similarity between the dark and the visible matter densities—i.e., $\Omega_{\rm DM}\sim\Omega_{\rm visible}$—in the Universe without fine tuning. The AQN is in many respects similar to Witten's quark nuggets (see Refs. [32–34] and the review in Ref. [35]). This type of DM candidate is "cosmologically dark" because of its small cross-section-to-mass ratio, not the weakness of its interactions. Namely, all quark nugget models have an excessively diffuse number density that obscures many observable consequences despite their strongly interacting nature. We refer to the original papers [36–39] devoted to the AQN formation, including the generation of the baryon asymmetry and the survival pattern, in the early Universe with its unfriendly environment; see also a recent brief review article [40] for many subtle questions on the formation mechanism. Here we mention several essential points to benefit the readers and make the presentation self-contained.

Compared to the original quark nugget models [32–35], the new element in the AQN model is the presence of the axion domain walls, which are copiously produced during the QCD transition.[1] The domain wall plays a dual role. First, it serves as an additional stabilization factor for the nuggets, which helps alleviate many problems with the original nugget construction [32–35]. Secondly, the same axion field $\theta(x)$ generates the strong and coherent $\mathcal{CP}$ violation in the entire visible Universe.

The inherent assumption in the AQN model is that the Peccei-Quinn (PQ) phase transition happens before inflation. Consequently, the initial misalignment angle $\theta_0\neq 0$ assumes one and the same value over the enormous scale of the visible Universe.[2] The axion field $\theta(x)$ can be treated as a classical $\mathcal{CP}$-violating field correlated on the scale of the entire Universe before the QCD epoch. The axion field starts to oscillate at the QCD transition by emitting the propagating axions. However, these oscillations remain coherent on the scale of the entire Universe. Therefore, the $\mathcal{CP}$-violating phase remains coherent on a global scale.

One related conceptual question would be why the baryons do not easily leak through the wide and flat axion domain. The answer is that the domain wall not only comprises axions but also mixes with the singlet η' field. This η' substructure has a narrow width of $\Lambda_{\rm QCD}^{-1}$ and interacts strongly with baryons. At the same time, it contributes negligibly to the surface tension of the domain wall. This coupling is a very generic feature of the system, because the axion and η' fields are phases of the same chiral condensate, and they interpolate between two physically identical (but topologically distinct) states as a combination of two knotted fields. The mixing also implies metastability of the domain walls, as the η' and the axion fields cannot be unknotted separately. Consequently, the axion domain wall (with the QCD substructure) is topologically stable even if it has a width (order of $m_a^{-1}\sim$ cm) much larger than the size of

---

[1] The axion is arguably the most compelling solution to the so-called strong $\mathcal{CP}$ problem (see original papers on the axion [41–47] and recent reviews [48–56]). As we will discuss, a globally coherent axion field is responsible for the baryon asymmetry in the early Universe. However, this source of $\mathcal{CP}$ violation is no longer available at the present time due to the axion dynamics.

[2] One should comment here that our scenario is dramatically different from conventional studies of the topological defects when PQ phase transition happens after inflation. In contrast, we assume the PQ phase transition happens before inflation, in which case the axion strings are not present in the system. However, the $N_{\rm DW}=1$ domain walls can be formed.

the quark nugget (order of 0.1 μm). To summarize, the presence of the η' substructure stabilizes the domain wall bubbles and prevents the baryon charge leakage.

Another conceptual question would be the evolution of these closed bubbles in the cosmic plasma. This complex dynamic problem involves immense differences in scale, such as the QCD scale Λ_{QCD}, the axion mass m_a, and the cosmic time $\sim 10^{-4}$ s at the QCD epoch. First, collapses of the closed $N_{\mathrm{DW}} = 1$ bubbles will be halted by the Fermi pressure from the accumulated fermions. Eventually, the $N_{\mathrm{DW}} = 1$ domain wall bubbles will become stable AQNs and compose the dark sector. Furthermore, the chemical potential inside the bubbles assumes a sufficiently large value $\mu_{\mathrm{form}} \gtrsim 400$ MeV during this long evolution; see the orange line in Fig. 2 of Ref. [39]. The magnitude of μ_{form} supports the AQN formation in the color superconducting (CS) phase. As mentioned above, the corresponding evolution is rather complex, as it includes three immensely different scales. Nevertheless, it leads to a consistent and coherent picture.

The other new element of the AQN model, which plays an absolutely crucial role for the present work, is that nuggets can be made of *matter* as well as *antimatter* during the QCD transition. Because of the coherent $\mathcal{CP}$ violation in the entire Universe, there is a preferential production of one species of the AQNs (i.e., the antimatter AQNs) over the other (i.e., the matter AQNs). The preference is determined by the sign of the initial misalignment angle θ_0 at the beginning of the AQN formation. Consequently, the dark and the visible matter densities will automatically assume the same order of magnitude—i.e., $\Omega_{\mathrm{DM}} \sim \Omega_{\mathrm{visible}}$—without fine tuning.

For the present studies, however, we take the agnostic viewpoint, and assume that such antimatter AQNs are present in our Universe today irrespective of their formation mechanism. This assumption is consistent with all presently available cosmological, astrophysical, and terrestrial constraints, as long as the average baryon charge of the nuggets is sufficiently large, as we review below.

One should emphasize that AQNs are absolutely stable configurations on cosmological scales. Furthermore, the antimatter which is hidden in the form of the very dense nuggets is unavailable for annihilation unless the AQNs hit the stars, planets, or interstellar medium.

However, when the AQNs hit the stars, planets, or interstellar medium, it may lead to observable phenomena. In particular, the injection of the energy due to the AQNs hitting the Sun may explain[3] the "solar corona heating problem" as advocated in Refs. [58–60]. There are also very rare events of annihilation in the Galaxy, which, in fact, may explain some observed Galactic excess emissions in different frequency bands, including very mysterious diffuse UV radiation [61,62], as recently argued in Ref. [63].

The strongest direct detection limit[4] is set by the IceCube Observatory; see Appendix A in Ref. [65]:

$$\langle B \rangle > 3 \times 10^{24} \quad [\text{direct (non)detection constraint}]. \tag{1}$$

Similar limits are also obtainable from ANITA and from geothermal constraints, which are also consistent with Eq. (1) as estimated in Ref. [66]. It has been also argued in Ref. [67] that AQNs producing a significant neutrino flux in the 20–50 MeV range cannot account for more than 20% of the DM density. However, the estimates [67] were based on the assumption that the neutrino spectrum is similar to the one which is observed in conventional baryon-antibaryon annihilation events, which typically produce a large number of pions and muons, and thus generate a significant number of neutrinos and antineutrinos in the 20–50 MeV range, where SuperK has a high sensitivity. However, the critical difference in the case of AQNs is that the annihilation proceeds within the color superconducting (CS) phase, where the energetics are drastically different [68]. The main point is that, in most CS phases, the lightest pseudo-Goldstone mesons (the pions and kaons) have masses in the 20 MeV range, rather than 140 MeV in the hadronic phase. This dramatically changes the entire spectrum such that the main assumption of Ref. [67] on the similarity of the neutrino's spectrum in both phases is incorrect. The resulting flux computed in Ref. [68] is perfectly consistent with observations. Furthermore, precisely these low-energy ($\lesssim$20 MeV) AQN-induced neutrinos produced in the Earth's interior might be responsible for the explanation of the long-standing puzzle of the DAMA/LIBRA observation of the annual modulation at a 9.5σ confidence level, as argued in Ref. [69].

The authors of Ref. [70] considered a generic constraint for the nuggets made of antimatter (ignoring all essential specifics of the AQN model such as the quark matter CS phase of the nugget's core). Our constraints [Eq. (1)] are consistent with their findings including the cosmic microwave background (CMB), big bang nucleosynthesis (BBN), and others, except for the constraints derived from the so-called "human detectors." As explained in Ref. [60], the corresponding estimates of Ref. [70] are oversimplified

---

[3] In fact, to resolve this problem, Parker conjectured long ago [57] that "nanoflares" are identified with the annihilation events in the AQN framework. The luminosity of the extreme UV (EUV) radiation from the corona due to these annihilation events is unambiguously determined by the DM density. It is a very nontrivial consistency check that the computed luminosity from the corona nicely matches with observed EUV radiation.

[4] Nondetection of etching tracks in ancient mica gives another indirect constraint on the flux of DM nuggets with mass $M >$ 55 g [64]. This constraint is based on the assumption that all nuggets have the same mass, which is not the case, as we discuss below. The nuggets with small masses represent a tiny portion of all nuggets in this model, such that this constraint is easily satisfied with any reasonable nugget's size distribution.

and do not have the same status as those derived from CMB or BBN constraints.[5]

While ground-based direct searches offer the most unambiguous channel for the detection of quark nuggets, the flux of nuggets is inversely proportional to the nugget's mass, and consequently, even the largest available conventional DM detectors are incapable of excluding the entire potential mass range of the nuggets. Instead, the large area detectors which are normally designed for analyzing the high-energy cosmic rays are much better suited for our studies of the AQNs, as we discuss next in Sec. II B.

B. AQNs entering the Earth

For our present work, however, the most relevant studies are related to the effects which may occur when the antimatter AQNs hit the Earth and continue to propagate deep underground in a very dense environment. In this case, most of the energy injection will occur in the Earth's interior. The corresponding signals are very hard to detect, as the photons, the electrons, and the positrons will be quickly absorbed by surrounding dense material deep underground, while the emissions of the very weakly interacting neutrinos and axions are hard to recover. Nevertheless, the AQN-induced axions from the deep interior can be recovered by analyzing the daily and annual modulations as suggested in Ref. [72] and elaborated in Ref. [73]. The AQN annihilation events in the Earth's atmosphere could produce infrasound and seismic acoustic waves as discussed in Refs. [71,74], when the infrasound and seismic acoustic waves indeed have been recorded by dedicated instruments. Furthermore, the AQN annihilation events explain the recently observed puzzling cosmic ray (CR)-like events such as the mysterious bursts observed by the Telescope Array (TA) [75,76], the exotic events observed by the Pierre Auger [77–79] and the very puzzling multimodal clustering events observed by the HORIZON 10T [80,81]. In these cases, the mysterious events can be explained as the AQN annihilation events as argued in Refs. [82,83] for the TA events, in Ref. [84] for the Pierre Auger exotic events, and in Ref. [85] for the multimodal clustering events.

Finally, the seasonal variations of the x-ray background in the near-Earth environment in the 2–6 keV energy range as observed by the XMM-Newton at the 11σ confidence level [86] may be also naturally explained within the same AQN framework as argued [87]. This application to the x-ray emission in the near-Earth environment is especially relevant for the present work, because the AQN-induced x rays according to the proposal [87] are originated from the AQN upward-going (Earth-emergent) events when the AQNs traverse through the Earth's interior and exit the Earth's surface.

Such events could, in principle, be responsible for the ANITA mysterious events [1–3] with exit angles of $-27°$ and $-35°$ relative to the horizon, as advocated in the present work. Before we present our arguments, we have to highlight in the next section the basic characteristics of the AQNs traversing the Earth, which is the topic of Sec. II C.

C. Upward-going (Earth-emergent) events

The goal here is to explain the basic features of the AQNs when they enter the dense regions of the surrounding material and annihilation processes start. The related computations originally have been carried out in Ref. [88] in application to the Galactic environment with a typical density of surrounding visible baryons of the order of $n_{\text{galaxy}} \sim 300\ \text{cm}^{-3}$ in the Galactic Center, in dramatic contrast with the dense region in the Earth's interior when $n_{\text{rock}} \sim 10^{24}\ \text{cm}^{-3}$. We review these computations with a few additional elements, which must be implemented in the case of propagation in the Earth's atmosphere and interior when the density of the environment is much greater than in the Galactic environment.

The total surface emissivity from the electrosphere has been computed in Ref. [88], given by

$$F_{\text{tot}} \approx \frac{16}{3}\frac{T^4\alpha^{5/2}}{\pi}\sqrt[4]{\frac{T}{m}}, \tag{2}$$

where $\alpha \approx 1/137$ is the fine structure constant, $m = 511$ keV is the mass of the electron, and T is the internal temperature of the AQN. One should emphasize that the emission from the electrosphere is not thermal, and the spectrum is dramatically different from blackbody radiation (see Ref. [88] and also Appendix A for more details).

A typical internal temperature of the AQNs for a very dilute Galactic environment can be estimated from the condition that the radiative output of Eq. (2) must balance the flux of energy onto the AQN

$$F_{\text{tot}}(4\pi R^2) \approx \kappa \cdot (\pi R^2) \cdot (2\ \text{GeV}) \cdot n \cdot v_{\text{AQN}}, \tag{3}$$

where n represents the number density of the environment. The left-hand side accounts for the total energy radiation from the AQN's surface per unit time as given by Eq. (2). The right-hand side accounts for the rate of annihilation events when each successful annihilation event of a single baryon charge produces $\sim 2m_p c^2 \approx 2$ GeV energy. In Eq. (3), we assume that the AQN is characterized by the geometrical cross section πR^2 when it propagates in

---

[5] In particular, the rate of energy deposition was estimated in Ref. [70], assuming that the annihilation processes between antimatter nuggets and baryons are similar to the $p\bar{p}$ annihilation process. It is known that this cannot be the case, because the annihilating objects have drastically different internal structures (hadronic phase versus CS phase). It has also been assumed in Ref. [70] that a typical x-ray energy is around 1 keV, which is much lower than direct computations in the AQN model would suggest [71].

an environment with a local density n with velocity $v_{\mathrm{AQN}} \sim 10^{-3}c$.

The factor κ is introduced to account for the fact that not all matter striking the AQN will annihilate, and not all of the energy released by an annihilation will be thermalized in the AQNs by changing the internal temperature T. In particular, some portion of the energy will be released in the form of the axions, the neutrinos, and the electron-positron pairs by the mechanism discussed below. In a neutral dilute environment considered previously [88], the value of κ cannot exceed $\kappa \lesssim 1$, which would correspond to the total annihilation of all impacting matter into thermal photons. The high probability of reflection at the sharp quark matter surface lowers the value of κ. The propagation of an ionized (negatively charged) AQN in a highly ionized plasma (such as the solar corona) will increase the effective cross section. As a consequence, the value of κ could be very large as discussed in Ref. [59] in application to the solar corona heating problem.

The internal AQN temperature had been estimated previously for a number of cases. It may assume dramatically different values, mostly due to the huge difference in the number density n entering Eq. (3). In particular, for the Galactic environment $T_{\mathrm{galaxy}} \approx 1$ eV, while in the deep Earth's interior it could be as high as $T_{\mathrm{rock}} \approx (100\text{–}200)$ keV. Precisely this value of T had been used as the initial temperature of the AQNs in the proposal [87] explaining the seasonal variations of the x rays observed by the XMM-Newton at the 11σ confidence level [86] at distances $r \sim (6\text{–}10)R_{\oplus}$ from the Earth's surface. The same temperature has also been used in Ref. [85] for explanation of the multimodal clustering CR-like events observed by the HORIZON 10T [80,81]. For our estimates in the present work, we shall use the same $T_{\mathrm{rock}} \approx (100\text{–}200)$ keV for explaining the AAEs.

One more feature we want to mention here and which is relevant for our present studies is as follows. There are many consequences of the high internal temperature $T \approx (100\text{–}200)$ keV, which results from annihilation processes as mentioned above. First, some positrons from the electrosphere may get excited and even leave the system, which obviously results in ionization of the AQN itself. Secondly, the e^+e^- pairs may be produced at such a high temperature, as the conventional suppression factor $\exp(-2m/T)$ is not dramatic for such T. This is the key element for the present work, as will be explained in the next section.

III. ANITA ANOMALOUS EVENTS AS UPWARD-GOING AQN EVENTS

We will now relate the AAEs to the upward-going AQN events with the specific features described in Sec. II. We highlight the primary ideas here and refer readers to Appendix A for technical details.

As mentioned, the AQNs propagating in the Earth's interior have a high temperature of 10^2 keV. This enables the production of e^+e^- pairs in the AQN's electrosphere. The e^+e^- pair production in a hot and dense environment has been studied previously in the context of the quark stars (see references in Appendix A). However, the developed technique does not apply to the present work, as the thermal equilibrium is absent in a small-size system such as the AQN. Thus, we will introduce a phenomenological parameter N, the number of the produced e^+e^- pairs at the moment of an AQN crossing the Earth's surface, in what follows.

The fates of an electron and a positron are entirely different in the background of an intense electric field. The electric field is coming from the ionization of the hot AQN. As estimated in Appendix A, the electric field repulses the created electrons and accelerates them to ultrarelativistic energy, $\langle E\rangle \sim 10$ MeV, as given by Eq. (A15). In contrast, the same electric field attracts the created positrons and traps them on the surface of the AQN. One should emphasize that these positrons created by pair productions have fundamentally different properties from those orbiting in the electrosphere [Eq. (A3)]. The orbiting positrons have much smaller bound energies and can locate far away from the surface of the AQN.

Consequently, we expect an instantaneous emission of energetic electrons with typical energy $\langle E\rangle \sim 10$ MeV, when the AQN emerges from the Earth's surface due to drastic perturbation. This instantaneous emission differs from when an AQN propagates in the Earth's deep interior. First, the emitted energetic electrons can propagate for several kilometers in the atmosphere and produce observable effects (e.g., geosynchrotron radiations). This is in contrast to when an AQN propagates underground, where the photons and the electrons will be quickly absorbed. Second, the electrons are dominantly emitted in the direction of the AQN velocity. This is because collisions and annihilations concentrate on the incident side of the AQN. As they are being created via pair production, the electrons are immediately accelerated along the direction of the background electric field, which approximately coincides with the direction of the AQN velocity. We also expect that the cross section of the incident collisions is given by the nugget's size R, which enters formula (3). This should be contrasted with a much larger size r^* of the electrosphere at high temperatures, as discussed in Appendix A.

Any precise computation of this instant of crossing is a very hard problem of nonequilibrium dynamics, which is beyond the scope of the present work. Fortunately, the observable radio signal (which is a direct consequence of the energetic emitted electrons) is not very sensitive to the details of this nonequilibrium mechanism and corresponding timescales, as it depends on several basic parameters, such as the typical energy $\langle E\rangle \sim 10$ MeV of the emitted electrons as estimated in Eq. (A15) and the number of emitted electrons N, as mentioned earlier. It is assumed that this number N will generate a coherent radio signal. The parameter N determines the intensity of the radiation, and it cannot be computed from first principles due to the very large uncertainties of the complicated nonequilibrium dynamics such as turbulence, shock waves, and strong ionization as mentioned above and further elaborated in Appendix A. This parameter must satisfy the constraint $N \ll N_{\max}$, where $N_{\max}$ is the maximal number of potentially available electrons [Eq. (A13)] which could be, in principle, liberated from the AQN at the instant of crossing the Earth's surface.

The number of electrons N which are emitted by a conventional cosmic ray shower of energy $E_{\mathrm{CR}} \sim (10^{17} - 10^{18})$ eV is of the order $N \sim (10^{8} - 10^{9})$. We anticipate a similar magnitude for the number of electrons $N \sim (10^{8} - 10^{9})$ emitted by AQNs as the observed intensity of the field strength for the anomalous ANITA events of order mV/m which agrees with the value of N, assuming the shower energy is $E_{\mathrm{CR}} \sim (10^{17} - 10^{18})$ eV.

Important arguments supporting our proposal that the AQN-induced events could mimic the anomalous radio signals observed by ANITA are based on very specific qualitative characteristics such as the spectrum and the pulse duration, rather than on a precise estimation of parameter N. The event rate of such anomalous events is also shown to be consistent with our AQN interpretation (see Sec. IV).

Furthermore, the average electron's energy in the energetic CR events with $E_{\mathrm{CR}} \sim (10^{17} - 10^{18})$ eV is around 30 MeV, which is in the same energy range of the AQN-induced electrons as estimated in Eq. (A15). Therefore, the electrons which are released as a result of AQN crossing the boundary in upward-going (Earth-emergent) events could mimic the radio signal of the conventional CR shower events as detected by ANITA. The topic of Sec. V will be the estimation of specific properties of the AQN-induced radio signal, such as the spectrum, the pulse duration, and the electric field strength.

IV. THE EVENT RATE OF AAEs

This section is devoted to estimating the event rate of AAEs within the AQN framework. It is expected to be a qualitative estimate up to an order-of-magnitude check due to large uncertainties in parameters and the rare occurrence of the observed AAEs. Nevertheless, we would like to present such an estimate to demonstrate that our interpretation of AAEs as a consequence of upward-going AQNs is at least a self-consistent proposal.

The expected number of AAEs, assuming that they are induced by the AQNs, can be estimated as follows:

$$\mathcal{N} \approx \mathcal{A}_{\mathrm{eff}} \mathcal{T} \Delta\Omega \frac{\mathrm{d}\Phi}{\mathrm{d}A \mathrm{d}\Omega}, \tag{4}$$

where $\mathcal{A}_{\mathrm{eff}} \approx 4\ \mathrm{km}^2$ is the effective area of ANITA [2], $\mathcal{T} \approx 48.75$ days is the combined exposure time of ANITA,[6] $\Delta\Omega \approx 2\pi$ for the isotropic flux of AQNs, and Φ is the total hit rate of AQNs on Earth [65]:

$$\Phi \approx 2.12 \times 10^{7}\ \mathrm{yr}^{-1} \left(\frac{\rho_{\mathrm{DM}}}{0.3\ \mathrm{GeV\,cm}^{-3}} \right) \times \left(\frac{v_{\mathrm{AQN}}}{220\ \mathrm{km\,s}^{-1}} \right) \left(\frac{10^{25}}{\langle B \rangle} \right), \tag{5}$$

where ρ_{DM} is the local density of DM. The local rate of upward-going AQNs per unit area depends on the flux distribution of the AQN:

$$\frac{\mathrm{d}\Phi}{\mathrm{d}A \mathrm{d}\Omega} = \frac{\eta}{4\pi R_{\oplus}^2} \Phi = 4 \times 10^{-2} \left(\frac{10^{25}}{\langle B \rangle} \right) \frac{\eta\,\mathrm{events}}{\mathrm{yr\,km}^2}, \tag{6}$$

where $R_{\oplus} = 6371$ km is the radius of the Earth, and η is a parameter that characterizes the local flux distribution of AQN. Specifically, $\eta \approx 1$ for isotropic distribution, and $\eta \approx 2$ for the so-called fixed-wind distribution based on the standard halo model so that more AQNs enter the Earth from the Northern Hemisphere and exit in the Southern Hemisphere [90]. Note that the survival rate of an AQN traversing through Earth is also taken into account in η implicitly, but it is an exceedingly minor effect compared to the flux distribution, because AQNs can penetrate through the Earth easily based on Monte Carlo simulation in Ref. [65].

Combining the estimates above, one should have

$$\mathcal{N} \approx 0.28 \left(\frac{\eta}{2} \right) \left(\frac{\rho_{\mathrm{DM}}}{0.3\,\mathrm{GeV\,cm}^{-3}} \right) \left(\frac{v_{\mathrm{AQN}}}{220\,\mathrm{km\,s}^{-1}} \right) \left(\frac{10^{25}}{\langle B \rangle} \right). \tag{7}$$

The expected number of events $\mathcal{N} \approx 0.3$ is almost 1 order of magnitude lower than $\mathcal{N}_{\mathrm{obs}} = 2$ events observed by ANITA. Nevertheless, we consider this order-of-magnitude estimation in Eq. (7) being consistent with our proposal due to many uncertainties which enter this estimate.

First, the parameters in Eq. (7) are in fact not precisely known. Essential parameters such as η, ρ_{DM}, $\langle v_{\mathrm{AQN}} \rangle$, and $\langle B \rangle$ only have accuracy up to order 1, as the local flux distribution of DM and the size distribution of AQN remain unknown to date. In fact, there are numerous hints suggesting that ρ_{DM} locally in the Solar System could be much larger from its canonical value; see a short comment on this with the references in the last paragraph of this section. Similarly, the effective area of detection $\mathcal{A}_{\mathrm{eff}}$ may double depending on the exit angle (see the estimate in, e.g., Ref. [19]), and the effective exposure time is potentially

---

[6] The effective exposure time was 17.25 days for ANITA-I [89], 7 days for ANITA-III [2], and 24.5 days for ANITA-IV [3], where we exclude ANITA-II (28.5 days), as it is not sensitive to upward-going air showers.

longer than our conservative estimate if we take into account the ANITA-II flight in the estimate (see footnote 6). In addition, the total number of observed AAEs could be a statistical fluctuation due to its rare occurrence (only 2).

We consider this order-of-magnitude estimate [Eq. (7)] as a highly nontrivial consistency check of our proposal, as the basic numerical factors entering Eq. (7) had been fixed from dramatically different physics (including the solar corona heating puzzle) and can easily deviate by a large factor. More importantly, our main arguments leading to the identification of the AAE with the AQN-induced radio pulses are based on specific qualitative features such as frequency dependence and duration of the pulse, which are not sensitive to these huge uncertainties in the normalization factor [Eq. (7)]. We consider the agreement between the observations and our theoretical estimates (to be discussed in Sec. V) for these specific characteristics as a strong argument supporting our identification.

It is also interesting to note that the extra numerical factor 0.1 (between the computed and observed values) which appears in our order of magnitude estimates in Eq. (7) is very similar to the extra factor 0.1 which occurred in analogous computations [82] of a number of mysterious bursts observed by the Telescope Array and similar estimates [85] of the event rate for puzzling multimodal clustering events observed by the HORIZON 10T instrument. This similarity hints at a common origin for all three phenomena, though the physics for these phenomena are dramatically different. This is because the main normalization factor representing the DM flux in the form of the AQN-induced events [Eq. (6)] is identical for all three estimates: for AAE [Eq. (7)], for the Telescope Array mysterious event count [82], and for multimodal clustering events [85]. If future studies support our identification of the AAE with the AQN-induced radio pulses, this numerical suppression factor might be a hint that the standard halo model (which is used in estimations for the DM flux) underestimates the local DM density in the Solar System. The true DM density locally may dramatically deviate from the average global value $\rho_{\rm DM} \approx 0.3\ \mathrm{GeV\,cm^{-3}}$; see the Introduction in Ref. [73] for references and details.

V. RADIO SIGNALS INDUCED BY AQNs

It is well known that the frequency spectrum of geosychrotron radiation emitted by an ultrarelativistic charged particle is equivalent to that emitted by a particle moving instantaneously at constant speed on an appropriate circular path with instantaneous radius of curvature ρ—see, e.g., Jackson [91]:

$$\rho \approx \frac{\gamma m c}{e\mathcal{B}\sin\theta_{\mathcal{B}}} \approx 0.8\ \mathrm{km}\left(\frac{\gamma}{20}\right), \tag{8}$$

where $\mathcal{B} \approx 0.5$ gauss is the local magnetic field strength, and $\theta_{\mathcal{B}}$ is the angle between the particle velocity $\mathbf{v}$ and the magnetic direction. We choose $\theta_{\mathcal{B}} \approx 60°$ in this work, as the magnetic field direction in Antarctica is approximately vertical, and the exit angles of the AAEs are typically of the order of 30°.

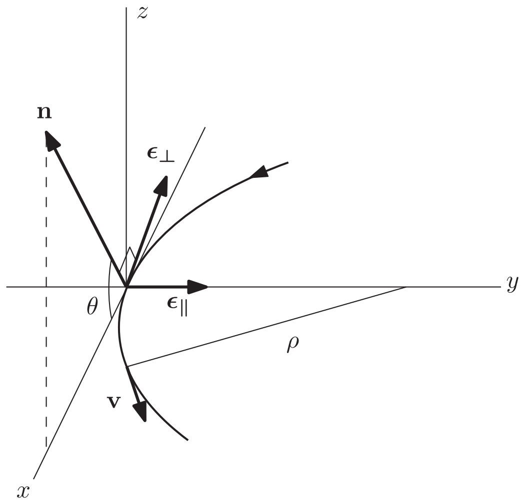

FIG. 1. The geometry of the emission, see description in the text.

The geometry follows from Fig. 1; the segment of trajectories lies in the x-y plane. The θ is the observation angle between $\mathbf{v}$ and the direction of the observer $\mathbf{n}$. An ultrarelativistic particle with Lorentz factor $\gamma \gg 1$ has a narrow emission angle $\theta \lesssim \gamma^{-1}$, beyond which the intensity of radiation is exponentially suppressed. $\boldsymbol{\epsilon}_\parallel$ and $\boldsymbol{\epsilon}_\perp$ are the two directions of polarization, as shown in Fig. 1.

For an observer with distance $\mathcal{R}$ from N coherent charged particles, the spectral component of the electric field $\mathbf{E}(\omega)$ as a function of frequency ω is given by [91]

$$|\mathbf{E}(\omega)| = N\left(\frac{4\pi}{c}\right)^{1/2}\frac{1}{\mathcal{R}}|\mathbf{A}(\omega)|,$$
$$\mathbf{A}(\omega) = \frac{-ie\omega}{\sqrt{8c\pi}}[-\boldsymbol{\epsilon}_\parallel A_\parallel(\omega) + \kappa\boldsymbol{\epsilon}_\perp A_\perp(\omega)], \tag{9}$$

where $A_\parallel(\omega)$ and $A_\perp(\omega)$ correspond to the amplitudes of two polarization directions in terms of modified Bessel functions:

$$A_\parallel(\omega) = i\frac{2\rho}{\sqrt{3}c}\left(\frac{1}{\gamma^2}+\theta^2\right)K_{2/3}(\xi), \tag{10a}$$

$$A_\perp(\omega) = \theta\frac{2\rho}{\sqrt{3}c}\left(\frac{1}{\gamma^2}+\theta^2\right)^{1/2}K_{1/3}(\xi), \tag{10b}$$

with

$$\xi = \frac{\rho\omega}{3c}\left(\frac{1}{\gamma^2}+\theta^2\right)^{3/2}. \tag{11}$$

Note that Eq. (10) is only well defined for $\omega > 0$; the values in the negative domain are defined by $\mathbf{A}(-\omega) = \mathbf{A}^*(\omega)$. The parameter κ in Eq. (9) is introduced to characterize the screening effect of the e^+e^- pair, where the $\boldsymbol{\epsilon}_\perp$ component is effectively canceled ($\kappa \approx 0$) when e^+e^- pairs are predominantly formed in conventional CR events [92]. In the opposite limit, we choose $\kappa \approx 1$ in the case of an AQN-induced signal, as it is primarily initiated by electrons such that the screening effect is diminished. The spectrum of the electric field is therefore

$$|\mathbf{E}(\omega)| \approx \sqrt{\frac{2}{3\pi}}\frac{Ne\rho\omega}{c^2\mathcal{R}}\left(\frac{1}{\gamma^2}+\theta^2\right)K_{2/3}(\xi) \times\sqrt{1+\frac{\gamma^2\theta^2}{1+\gamma^2\theta^2}\left(\frac{K_{1/3}(\xi)}{K_{2/3}(\xi)}\right)^2}. \qquad (12)$$

The observational distance from the ANITA balloon payload is of the order of 35 km, and the size of the detector is of the order of 10 m; therefore, the effective observation angle is tiny compared to the emission angle $\theta \sim 10^{-4} \ll \gamma^{-1}$.

Choosing $\theta = 0$, we plot the spectrum [Eq. (12)] in Fig. 2 with different values of γ for a specific value of $N = 5\times 10^8$. One can see that the spectrum is very flat: the absolute value $|\mathbf{E}(\omega)|$ changes by a factor of 3 or so when the frequency ν varies by 2 orders of magnitude. Furthermore, the total strength of the electric field integrated over the entire frequency band agrees with the observed value on the level of $|\mathbf{E}| \sim \mathrm{mV/m}$; see Refs. [1–3].

Another generic feature of synchrotron radiation is the exponential suppression of the emission beyond the critical frequency [91]

$$\nu_c \equiv \frac{3\gamma^3 c}{4\pi\rho} \approx 0.7\ \mathrm{GHz}\left(\frac{\gamma}{20}\right)^2. \qquad (13)$$

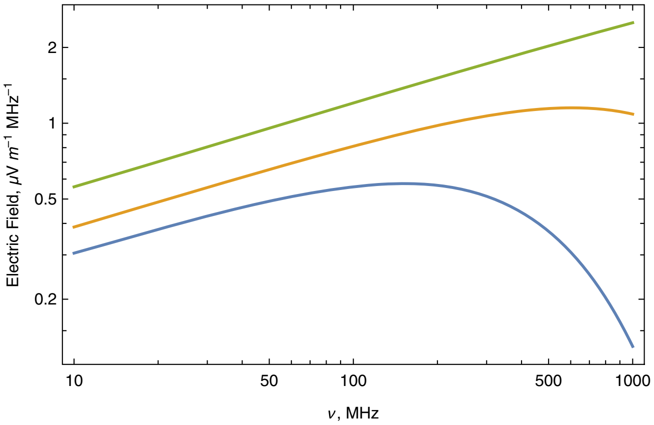

FIG. 2. Spectrum of electric field $|E(2\pi\nu)|$ from Eq. (12), with $\theta = 0$, $\mathcal{R} = 35$ km, and $N = 5\times 10^8$. The Lorentz factor is chosen to be $\gamma = 10$ (blue), 20 (orange), and 60 (green).

This qualitative consequence of our proposal is also consistent with ANITA observations [1–3].

The time-dependent radio pulse can be reconstructed from the frequency spectrum by an inverse Fourier transform:

$$\mathbf{E}(t) = \frac{1}{\sqrt{2\pi}}\int_{-\infty}^{\infty} b(\omega)\mathbf{E}(\omega)e^{-i\omega t}\mathrm{d}\omega \approx -\boldsymbol{\epsilon}_\parallel \frac{2Ne\rho}{\sqrt{3\pi c^2\gamma^2\mathcal{R}}}\mathrm{Re}\left[\int_0^\infty b(\omega)\omega \mathrm{K}_{2/3}(\xi)e^{-i\omega t}\mathrm{d}\omega\right], \qquad (14)$$

where $b(\omega)$ is the filter characterizing the receiver, similar to the analysis in Ref. [92]. For illustrative purposes, we plot the time-dependent electric field in Fig. 3 by assuming an idealized rectangle filter spanning (40–80) MHz and (200–600) MHz. The pulse has an amplitude $|\mathbf{E}_0| \sim \mathrm{mV/m}$ and the time duration $\tau \sim \mathrm{ns}$, which is consistent with observed features of the anomalous pulses observed by ANITA [1–3]. Because $|\mathbf{E}(\omega)|$ is approximately flat in the frequency range below ν_c, $\mathbf{E}(t)$ is essentially determined by the inverse Fourier transform of $b(\omega)$. In the case of a rectangle-like filter with frequency bandwidth $\Delta\nu$, the time duration of the pulse is determined by $\Delta\nu$ as follows:

$$\tau \approx \frac{1}{\Delta\nu} \approx 2\ \mathrm{ns}\left(\frac{600\ \mathrm{MHz}}{\Delta\nu}\right). \qquad (15)$$

The numerical value for the timescale τ is not very sensitive to the parameters of the model as explained above due to the flatness of the spectrum below ν_c. In contrast to the time duration τ, the absolute value of the electrical field $|\mathbf{E}_0| \sim \mathrm{mV/m}$ is sensitive to γ, as shown in Fig. 3. It assumes the values which are also consistent with observations [1–3].

It is instructive to understand the temporal features of the electric field $\mathbf{E}(t)$ by rewriting the integral (14) in terms

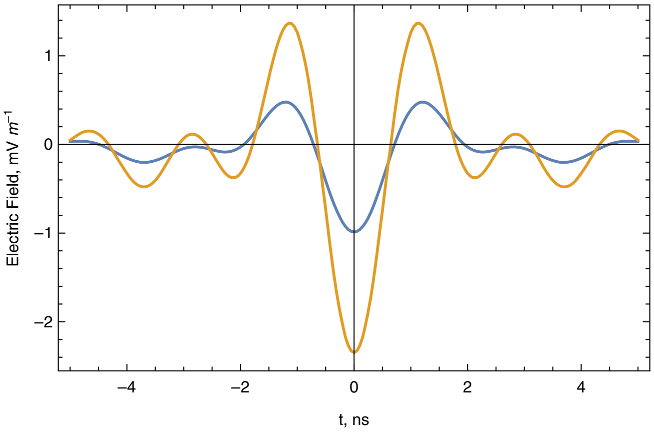

FIG. 3. Time-dependent electric field from Eq. (14) with $\theta = 0$, $\mathcal{R} = 35$ km, and $N = 5\times 10^8$, using an idealized rectangle filter. The Lorentz factor is chosen to be $\gamma = 10$ (blue) and 20 (orange). Filters: (40–80) MHz and (200–600) MHz.

of the dimensionless variable ξ defined by Eq. (11) as follows:

$$\mathbf{E}(t) = -\boldsymbol{\epsilon}_{\parallel} \frac{18}{\sqrt{3}\pi\rho} \frac{\gamma^4 Ne}{\mathcal{R}} \mathrm{Re}\left[\int_{\xi_{\min}}^{\xi_{\max}} \xi e^{-ia\xi} \mathrm{K}_{2/3}(\xi) \mathrm{d}\xi\right], \quad (16)$$

where we portray $b(\omega)$ as an idealized rectangle filter, where $a \equiv 3\gamma^3 ct/\rho$ and $(\xi_{\min}, \xi_{\max})$ are determined by corresponding values of $\omega_{\min}$ and $\omega_{\max}$ characterizing the filter $b(\omega)$. From Eq. (16), one can explicitly see that the typical time duration is determined by the parameter

$$(a\xi) \approx 2\pi \quad \Rightarrow \quad \tau \approx (2-4) \text{ ns}, \quad (17)$$

and the combination $(a\xi)$, which is the phase entering Eq. (16), is indeed γ-independent for $\theta \ll \gamma^{-1}$.

The same formula (16) also shows that the absolute value of the field $\mathbf{E}(t)$ and the time duration is mostly determined by the region of the largest values of ξ close to $\xi_{\max}$, while the low-energy portion of the spectrum does not play a role. We explicitly check this feature by plotting in Fig. 4 the electric field $\mathbf{E}(t)$ with two different models for the filter. The solid line includes both filters spanning the low- and high-frequency modes, while the dashed line corresponds to a single filter describing exclusively high-frequency modes. The difference between the two curves is negligible, as claimed. Another property worth mentioning is that the absolute value of the field $\mathbf{E}(t)$ in the peak increases with the extension of the upper value for $\omega_{\max}$ to higher values (800 MHz in Fig. 4 versus 600 MHz in Fig. 3). This is also expected behavior, as the integral (16) is saturated by the region of the largest values of ξ close to $\xi_{\max}$, as already mentioned.

The AQN-induced signal is in many aspects similar to the conventional CR shower, with the crucial and dramatic difference being the *noninverted polarity*. It well matches the observation of the anomalous events in the ANITA experiment. We list a number of distinct features (between AQN-induced events and conventional CR air showers events) in Sec. VI.

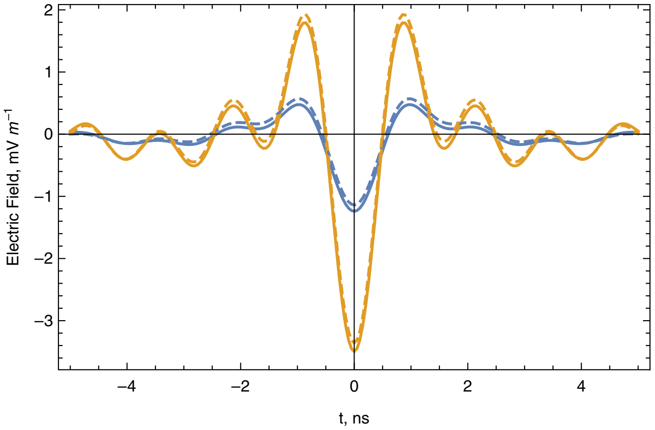

FIG. 4. Time-dependent electric field from Eq. (14) with $\theta = 0$, $\mathcal{R} = 35$ km, and $N = 5 \times 10^8$, using an idealized rectangle filter. The Lorentz factor is chosen to be $\gamma = 10$ (blue) and 20 (orange). Solid line: Two filters spanning (40–80) MHz and (200–800) MHz. Dashed line: Single filter at (200–800) MHz.

For completeness, we also derive the spectrum of power emission similarly to the estimate in Ref. [92]. The power is related to the electric field by the Poynting vector:

$$\mathbf{S}(t) = \frac{c}{4\pi} \mathbf{E}(t) \times \mathbf{B}(t), \quad (18)$$

where we use the Gaussian units. The power density is given by

$$\frac{\mathrm{d}P(t)}{\mathrm{d}A} = |\mathbf{S}(t)| = \frac{c}{4\pi} |\mathbf{E}(t)|^2. \quad (19)$$

Averaging over the time duration of the pulse τ gives

$$\left\langle \frac{\mathrm{d}P(t)}{\mathrm{d}A} \right\rangle_\tau = \frac{c}{4\pi\tau} \int |\mathbf{E}(t)|^2 \mathrm{d}t \approx \frac{c}{4\pi\tau} \int |\mathbf{E}(\omega)|^2 \mathrm{d}\omega, \quad (20)$$

where the last step follows from Parseval's theorem. The spectrum of the power density is therefore

$$\frac{\mathrm{d}^2 P}{\mathrm{d}\omega \mathrm{d}A} \approx \frac{\mathrm{d}}{\mathrm{d}\omega} \left\langle \frac{\mathrm{d}P(t)}{\mathrm{d}A} \right\rangle_\tau \approx \frac{c}{4\pi\tau} |\mathbf{E}(\omega)|^2. \quad (21)$$

The spectrum for the power of the emission shares similar properties to that of the electric field, as it is expressed in terms of the electric field $|\mathbf{E}(\omega)|$. The results for the power density are presented in Fig. 5, where we use $\tau \approx 4$ ns for numerical estimates taken from Eq. (17), Fig. 3, and Fig. 4. This value is also consistent with ANITA observations shown in Fig. 2 of Ref. [2]. The power density is of the order of $(0.2-0.3)$ pW m^{-2} MHz^{-1} for $\gamma = 20$ and frequencies $\nu \gtrsim 100$ MHz, and then it falls

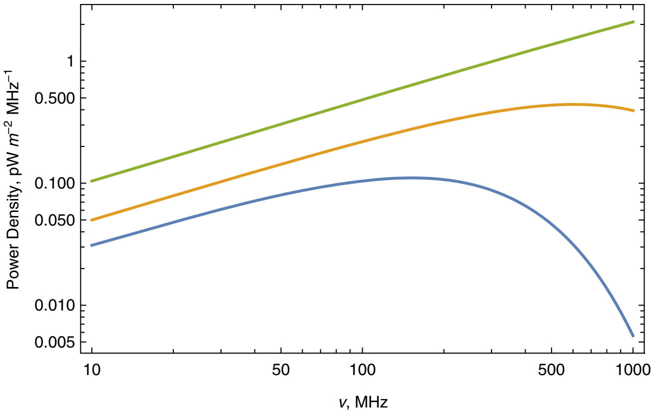

FIG. 5. Spectrum of power density from Eq. (21), with $\tau = 4$ ns, $\theta = 0$, $\mathcal{R} = 35$ km, and $N = 5 \times 10^8$. The Lorentz factor is chosen to be $\gamma = 10$ (blue), 20 (orange), and 60 (green).

sharply beyond the critical frequency [Eq. (13)]. This behavior is consistent with ANITA's results presented in Fig. 4 of Ref. [2].

We finish this section with a few comments on the accuracy of our estimates. It should be emphasized that the computations carried out in this section are oversimplified, as realistic signals can be severely modified by numerous factors such as the geometry of the beam, the relative position of the observer, and the frequency characteristics of the receiver's filters [92,93]. Nonetheless, most factors, such as lateral structure and inclined axis of the beam, are near-field effects, and they are eliminated since the observation angle is small. There are many other factors, such as the electron energy distribution of the beam as a function of γ, that may modify our predictions. We cannot predict the corresponding behavior, as it is determined by very complex nonequilibrium dynamics, as discussed in Appendix A.

VI. CONCLUSION AND FUTURE DEVELOPMENT

Our basic results can be summarized as follows. We explore a new possible explanation for the AAEs [1–3] by suggesting that these events can be related to the DM annihilation events within the AQN framework. To be more precise, we argued that these events can be interpreted as the AQN-induced radio pulses which result from the AQN traversing the Earth and going in the upward direction. The basic qualitative characteristics (such as the emission frequency, the electric field strength, and the radio pulse durations as presented in the Sec. V) of the observed AAEs are consistent with our AQN interpretation.

One should mention that the AQN-induced radio pulses can be easily discriminated from conventional sources, such as CR air showers [92,93].

Indeed, a "rule of thumb" suggests that the maximal number of charged particles (mostly electrons and positrons) in a CR air shower is $E_{\rm CR}/{\rm GeV}$, which implies that $N \approx (10^8 - 10^9)$ for an $E_{\rm CR} \approx (10^{17} - 10^{18})$ eV shower (see, e.g., Ref. [92]). This number of electrons from the CR shower is close to the number of electrons being emitted by the AQN according to Eq. (A13). Furthermore, the typical average energy in the CR shower is 30 MeV, which is also very similar to our estimates for the AQN-induced spectrum of the electrons with $E \in (1\text{–}10^2)$ MeV with the peak around 10 MeV according to Eq. (A13). Therefore, it should not be a surprise that the radio emission intensity and the electric field strength are very similar in both cases, as the geomagnetic field $\mathcal{B} \approx 0.5$ gauss (which represents the source of the acceleration and consequent radio emission) is obviously the same in the same location.

Now, we want to discuss the drastic differences between the pulses induced by conventional CR showers and the AQNs. These dramatic distinct features can be tested in future experiments such that our proposal can be discriminated from other suggestions. We list below the following typical spectral features of the CR-induced radio pulses and contrast them with the AQN-induced radio pulses:

1. The generic spectral feature of the CR-induced radio emission is the presence of oscillations, which normally starts around 100 MHz (depending on the distance from the shower axis); see, e.g., Fig. 1 in Ref. [93]. These oscillations are due to the coherence diminishing as the wavelength becomes shorter (in comparison to the "pancake" size in the CR shower). While it is obviously affected by the detector's filter, this feature is a physical effect due to the changing number of coherent particles with different wavelengths. Such a picture being typical for the CR-induced radio emission is not expected to occur for the AQN-induced radio signal, as the notion of a "pancake" does not exist in our case; see also item 3 below with an argument that the notion of a "central axis" does not exist for the AQN-induced events.
2. Another typical feature of the CR-induced radio emission is that most of the power is emitted at frequencies around (20–30) MHz for an $E_{\rm CR} \approx 10^{17}$ eV shower (see Fig. 2 in Ref. [93]). This is the result of a very strong cutoff frequency $\nu_0 \lesssim 50$ MHz, which strongly depends on features of the shower; see Eqs. (2) and (12) in Ref. [93]. It should be contrasted with our case when the cutoff frequency $\nu_{\rm c} \sim 0.7$ GHz is determined by dramatically different physics, as expressed by Eq. (13).
3. The final and most important difference between these two cases is that the cutoff frequency ν_0 in CR air showers strongly depends on many parameters of the shower, such as the distance from the central axis when the number of particles per unit area strongly depends on this parameter. It must be contrasted with our case of the AQN-induced radio signal when all electrons emitted from the same point at the same instant are moving along the same direction.

This picture suggests that the event could be viewed as a uniform front of size $\rho \sim 0.8$ km defined by Eq. (8) rather than a CR air shower with a well-defined central axis. In different words, the number of particles per unit area in the bunch of electrons does not depend on the distance from the central axis, in huge contrast with conventional CR air showers. The notion "central axis" simply does not exist for the AQN-induced electrons, as the number of particles per unit area is approximately the same for all electrons generating the radio pulse.

These features of the AQN-induced radio events are very distinct from conventional CR-induced radio pulses, and they should be easily discriminated by future analyses with more quality data. This can be achieved, for example, by placing two or more independent but synchronized antennas at a distance to study the same events from different locations. It would allow us to test many ideas advocated in the present work, including some features of the AQN-induced radio emission which are not shared by conventional CR air showers, as discussed in items 1–3 above. If future studies indeed support and substantiate our proposal, it would be a strong argument supporting the AQN nature of the AAEs.

We conclude by mentioning that many other instruments can test the AQN model, as mentioned in Secs. II A and II B. There are several other instruments mentioned in Refs. [94,95] that can test the macroscopically large AQN-type models. However, it may require proper adjustment of the bin time of the detectors, as argued in Ref. [94]. We elaborate on this problem in Appendix B, given several constraints recently published by the Pierre Auger Collaboration [96,97] on upward-going showers. As concluded in Appendix B, the constraints [96,97] rely on the assumption that the upward-going showers are seeded by primary particles with ultrarelativistic energy $E \approx (10^{16.5} - 10^{18.5})$ eV, similarly to conventional down-going showers. This assumption does not apply to our proposal, because AQNs move with a nonrelativistic speed $v_{\rm AQN} \sim 10^{-3}c$, so the event reconstruction qualitatively differs from those with light speed; see Appendix B for details.

ACKNOWLEDGMENTS

This research was supported in part by the Natural Sciences and Engineering Research Council of Canada, and X. L. also by the UBC four-year doctoral fellowship.

APPENDIX A: SOME TECHNICAL DETAILS ON THE AQN PROPERTIES

In this appendix, we want to estimate the parameters which enter the formulas in the main body of the text. We want to estimate parameters such as mean free path λ; typical distance r^*, where e^+e^- are mostly produced and the electrons may leave the system; typical electric field; electric potential at distance r^*; etc.

One should emphasize that the following evaluations will be order-of-magnitude estimations, at the very best, due to many uncertainties present in the system. One of the challenges is the nonperturbative QCD in the strongly coupled regime. For example, the phase diagram in this regime is not even known, as mentioned in Sec. II A. The other challenge is the complex interaction in a nonequilibrium dynamic system. For example, a moving AQN can generate turbulence and shock waves due to its large Mach number $M = v_{\rm AQN}/c_s$. Hence, the analysis cannot be exact, even though the AQN model has very few fundamental parameters, such as the size R and the baryon charge B.

We start by mentioning that pair production of e^+e^- can occur in a dense and hot environment, which has been discussed in the context of quark stars at $T \gtrsim 10^2$ keV (see Refs. [98–104]). In the context of the present work, all the key ingredients relevant for e^+e^- production are also present in the system. For instance, the AQN is characterized by a similar temperature $T \gtrsim 10^2$ keV. Moreover, the quark core is assumed to be in the CS phase. Lastly, there is a strong electric field in the system. However, we cannot use the results from the previous studies obtained in the context of the quark stars. This is because the size of the AQN is much smaller than the relevant mean free paths for all elementary processes, as discussed below. As a result, thermal equilibrium cannot be achieved in the AQN system, and the nonequilibrium dynamics determine the entire physics in the high-temperature regime. It should be contrasted with large quark stars, where the thermal equilibrium is maintained.

Nevertheless, it is instructive to review the relevant results from the previous studies [98–104] on quark stars for the following reasons. First, the main ingredients in a quark star system and in our present study are similar, such as the high temperature, the dense quark matter physics, and the strong electric field. Second, the complexity of the computation can be demonstrated in a much simpler case—the bare quark stars where thermal equilibrium is maintained, which remains controversial 25 years after the original paper [98].

It was originally suggested in Refs. [98,99] that the quark stars can emit e^+e^- pairs. References [98,99] considered a typical temperature $T \gtrsim 10^2$ keV, which is consistent with the condition in our proposal, as mentioned in Sec. II B. In Refs. [100,101], the authors argued that bremsstrahlung radiation from the electrosphere could be much more important than e^+e^- emission. Furthermore, the emission rate could be dramatically modified by several effects, such as the boundary effects, the inhomogeneity of the electric field, and the Landau-Pomeranchuk-Migdal suppression. In Ref. [102], it was suggested that the Pauli blocking would strongly suppress the bremsstrahlung emission. More recent studies in Refs. [103,104] argued that the so-called mean-field bremsstrahlung could be the dominant mechanism.

We are not attempting to analyze all these suggested emission mechanisms critically. Instead, our goal is to mention that even a relatively simple system of the bare quark star being in equilibrium remains a matter of debate. The AQN emission at high temperatures is even more complicated due to the nonequilibrium dynamics.

We start by mentioning that the density of positrons $n(z,T)$ in the electrosphere for the Galactic environment (low temperature) at distance z from the nugget's surface has been computed in the mean field approximation in Ref. [88]. It has the following form:

$$n(z,T) = \frac{T}{2\pi\alpha}\frac{1}{(z+\bar{z})^2}, \tag{A1}$$

where $\bar{z}$ is the integration constant chosen to match the Boltzmann regime at sufficiently large $z \gg \bar{z}$. Numerical studies [105] support the approximate analytical expression in Eq. (A1):

$$\bar{z}^{-1} \approx \sqrt{2\pi\alpha} \cdot m \cdot \left(\frac{T}{m}\right)^{\frac{1}{4}}, \qquad n(z=0) \approx (mT)^{\frac{3}{2}}. \tag{A2}$$

In the equilibrium with a small annihilation rate typical for the Galactic environment, the positrons will normally occupy a very thin layer on the order of $\bar{z}$ around the AQN's quark core, as computed in Refs. [88,105]. However, in our case, when the AQN enters the Earth's atmosphere, and further, the interior, a large number of nonequilibrium processes as mentioned above are expected to occur. Furthermore, the positron cloud is expected to expand well beyond the thin layer around the nugget's core as a result of the direct collisions with Earth material, in which case some positrons will be kicked off and leave the system. In this case, the one-dimensional expression (A1) does not apply at distance $r \gtrsim R$, as excited positrons will be far away from the core—i.e., at distance $r \gg R$.

To proceed with our estimates, we assume that the density $n(r,T)$ has a powerlike behavior at $r \gtrsim R$ with exponent p. This assumption is consistent with our numerical studies [105] of the electrosphere with $p \approx 6$. It is also consistent with the conventional Thomas-Fermi model at $T = 0$—see, e.g., the Landau textbook.[7] We consider parameter p to be arbitrary in order to demonstrate that our main claim is not very sensitive to our assumption on the numerical value of p.

Therefore, we parametrize the density as follows:

$$n(r,T) \approx n(z=0)\left(\frac{R}{r}\right)^{p}, \qquad R \approx 2\times 10^{-5}\ \mathrm{cm}$$
$$n_0 = n(z=0) \approx 0.16\times 10^{31}\left(\frac{T}{100\ \mathrm{keV}}\right)^{\frac{3}{2}}\ \mathrm{cm}^{-3}, \tag{A3}$$

where $n_0 \equiv n(z=0)$ is the positron density determined by Eq. (A2). The density profile (A3) allows us to estimate the effective charge of the nugget $Q_{\mathrm{eff}}(r^*)$ at distance $r^* \gg R$, assuming that $Q_{\mathrm{eff}}(r^*)$ is much greater than the number of positrons removed from the system.[8] The corresponding $Q_{\mathrm{eff}}(r^*)$ can be estimated by integrating from r^* to infinity instead of accounting for the cancellations between the original negative charge of the antimatter AQN and positive charge of the surrounding positrons—i.e.,

$$Q_{\mathrm{eff}}(r^*) \approx \int_{r^*}^{\infty} 4\pi r^2 n(r)\mathrm{d}r \sim \frac{4\pi n_0 R^3}{(p-3)}\left(\frac{R}{r^*}\right)^{p-3}$$
$$\approx 10^{11}\left(\frac{2\times 10^{-3}\ \mathrm{cm}}{r^*}\right)^{3} \quad \text{for } p \approx 6. \tag{A4}$$

In estimate (A4), we assumed that the power behavior in Eq. (A3) holds in this regime. The relevant parameter is the charge-to-mass ratio Q_{eff}/M, which is 14 orders of magnitude smaller for the AQNs compared to a similar ratio e/m_p computed for the proton. Indeed, the AQN's mass is of order $M \approx m_p B$ with a typical baryon charge $B \sim 10^{25}$, while $Q_{\mathrm{eff}} \sim 10^{11}$.

Our next task is to estimate the binding energy $U(r^*)$ of the positrons at the distance r^* as follows:

$$U(r^*) = \frac{\alpha Q_{\mathrm{eff}}(r^*)}{r^*} \approx 10\ \mathrm{MeV}\left(\frac{2\times 10^{-3}\ \mathrm{cm}}{r^*}\right)^{4}. \tag{A5}$$

Here we choose $r^* \approx 2\times 10^{-3}$ cm for reasons to be explained later in this appendix. This estimate suggests that if an electron will be created at distance $r^* \approx 2\times 10^{-3}$ cm, it will be quickly accelerated up to energies on the order of 10 MeV as a result of strong repulsion due to the Coulomb force [Eq. (A5)]. These parameters are used for estimations in the main text in Sec. III. We shall argue below that this value $r^* \approx 2\times 10^{-3}$ cm is indeed an appropriate scale, beyond which the electrosphere becomes transparent to electrons created via pair production.

To make our arguments more convincing, we have to estimate a number of effects related to this physics. In particular, we have to estimate the rate of e^+e^- production at this distance r^*, the electron's mean free path $\lambda(r^*)$, the screening length, the equilibration time, and many other characteristics which support our proposal.

We start with the estimation of the e^+e^- density in the environment at temperature T, assuming that thermal equilibrium conditions are fulfilled. The corresponding density of the electrons n_- and positrons n_+ is given by the conventional Fermi distribution [107]:

$$n_+ = n_- = \frac{1}{\pi^2}\int_0^{\infty} \frac{p^2 dp}{e^{\epsilon/T}+1}, \qquad \epsilon = \sqrt{p^2+m^2}, \tag{A6}$$

where the much smaller background positron density $n(r^*)$ from Eq. (A3) has been ignored in the estimates of Eq. (A6). At very low temperatures T, the number densities are suppressed by a factor of $\exp(-m/T)$. This is because the number density of energetic photons capable of producing massive particles is exponentially small.

Formula (A6) is valid only in the large-volume limit so that thermal equilibrium can be maintained. By "large volume," we mean that we require all mean free paths for all processes be much smaller than the size of the system V.

---

[7] In the notations of Ref. [106], the dimensionless function $\chi(x)$ behaves as $\chi \sim x^{-3}$ at large x. The potential $\phi = \chi(x)/x$ behaves as $\phi \sim x^{-4}$. The density of electrons in the Thomas-Fermi model scales as $n \sim \phi^{3/2} \sim x^{-6}$ at large x.

[8] This assumption is essentially equivalent to the expectation that the positrons removed from the system were localized at much larger distances, which is indeed the case. For example, the corresponding scale $R_{\mathrm{cap}} \approx 1$ cm from Ref. [82] is indeed much greater than the scale $r^* \approx 10^{-3}$ cm, which is the relevant scale of the problem to be discussed in this work.

However, this condition is not satisfied in our case of a small nugget, as we will argue below.

In particular, the typical cross sections for $\gamma\gamma \to e^+e^-$, $e^+e^- \to \gamma\gamma$, and $\gamma e^\pm \to \gamma e^\pm$ are on the order of

$$\sigma_{\gamma\gamma\to e^+e^-} \sim \sigma_{e^+e^-\to\gamma\gamma} \sim \sigma_{\gamma e^\pm\to\gamma e^\pm} \sim \pi r_0^2, \qquad r_0 = \frac{\alpha}{m} \approx 2.8 \times 10^{-13}\ \text{cm} \tag{A7}$$

at relativistic velocities and temperature $T \approx 100$ keV. The mean free path for these processes can be estimated as follows:

$$\lambda \sim \frac{1}{\sigma n_\pm} \sim 2.5 \times 10^{-3}\ \text{cm}, \tag{A8}$$

which is the same order of magnitude as the r^* entering Eqs. (A4) and (A5). This observation obviously implies that the thermal equilibrium cannot be maintained in a small volume $V \sim (r^*)^3$ if $r^* \ll \lambda$.

Another process that equilibrates the system is the Coulomb elastic scattering with cross section $\sigma_{\rm Coul}$ estimated as follows:

$$\sigma_{\rm Coul} \approx \frac{\alpha^2}{E^2\theta^4} \approx 0.8 \times 10^{-25} \left(\frac{1}{\theta}\right)^4 \left(\frac{m}{E}\right)^2\ \text{cm}^2, \tag{A9}$$

which is essentially the same order of magnitude as Eq. (A7) for $\theta \sim 1$. Furthermore, the processes related to $\sigma_{\rm Coul}$, $\sigma_{e^+e^-\to\gamma\gamma}$, and $\sigma_{\gamma e^\pm\to\gamma e^\pm}$ decrease at large energies as E^{-2} as explicitly shown in Eq. (A9), which makes the typical λ estimated in Eq. (A8) much greater at larger energies:

$$\lambda(E) \sim \frac{1}{\sigma(E) n_\pm} \sim 8 \times 10^{-3} \left(\frac{E}{m}\right)^2\ \text{cm}. \tag{A10}$$

We mention dependence $\lambda(E)$ on energy E because the key element of our proposal is the fast acceleration of the produced electrons due to the strong background repulsive (for electrons) electric field determined by Eq. (A5). Our estimates above strongly suggest that the electrons produced by this mechanism can be accelerated up to 10 MeV energy without much scattering. This is because $\lambda(E)$ is much larger than the size $r^* \sim 10^{-3}$ cm of the accelerating region.

Similar arguments also suggest that there is a suppression factor $(r^*/\lambda)^3 \ll 1$ if $\lambda \gg r^*$. This factor accounts for the "reduced" equilibration volume, violating the basic requirement for maintaining the thermodynamical equilibrium for $\lambda \gg r^*$.

To make this argument more quantitative, we estimate r^* from the requirement $\lambda \approx r^*$, which determines the numerical value of $r^* \approx 2 \times 10^{-3}$ cm entering Eqs. (A4) and (A5).

There is an additional suppression related to dramatically different timescales: the typical time for the equilibration λ/c is much longer than the typical time of the electron's acceleration to relativistic velocity, which is $t_0 \sim mr^*/U(r^*)$. After this short period of time t_0, the accelerated electrons are lost for equilibration with other particles. Accounting for both these effects, the maximal number of e^+e^- pairs being produced by this mechanism in volume $V \sim (r^*)^3$ can be estimated as follows:

$$[n_\pm \cdot V] \cdot \left(\frac{r^*}{\lambda}\right)^3 \cdot \left(\frac{t_0 c}{\lambda}\right) \sim 10^{15}, \qquad V \sim (r^*)^3. \tag{A11}$$

Another possible suppression factor could be due to a strong overestimation of the effective volume in Eq. (A11) approximated as $V \sim (r^*)^3 \sim \lambda^3$. The point is that the γ radiation and accompanied pair production of e^+e^- from this region become the dominant cooling mechanism only in the vicinity where the quark-antiquark pair gets annihilated within a small area πR^2. The equilibration time λ/c is too long to distribute this heat over the entire volume $V \sim (r^*)^3$ sufficiently quickly before the particles leave the system. Therefore, we expect an additional suppression factor in Eq. (A11) which accounts for this effect:

$$\left(\frac{R}{r^*}\right)^2 \sim 10^{-4}. \tag{A12}$$

Accounting for this additional suppression further reduces the estimate in Eq. (A11) for the maximal number of available electrons:

$$N_{\rm max} \sim [n_\pm \cdot V] \left(\frac{r^*}{\lambda}\right)^3 \left(\frac{t_0 c}{\lambda}\right) \left(\frac{R}{r^*}\right)^2 \sim 10^{11}. \tag{A13}$$

In addition to these suppression factors, there are a number of many-body effects which may modify the estimate in Eq. (A13). For example, there is Debye screening, with the corresponding length λ_D being defined by the formula

$$\lambda_D \approx \sqrt{\frac{T}{4\pi\alpha n(r,T)}}, \tag{A14}$$

where $n(r,T)$ is the background positron density determined by Eq. (A3).

The Debye screening normally applies to the situation when a single external charge q is inserted into the plasma. In this case, the charge q will be screened on the scale of λ_D—i.e., $q\exp(-r^*/\lambda_D)$. There are a few assumptions for the Debye screening to be operational. First of all, the elementary processes responsible for the screening should be much faster than the typical timescales of a slowly moving external charge q. Second, the density of the external charges q must be much smaller than the density of the charged particles in the surrounding plasma. Both assumptions are not justified in our case when we treat the produced electrons as the inserted external charges.

Indeed, the mean free path of the positrons from the electrosphere, which are capable of screening the emitted electrons, is $\lambda^{-1}(r^*) \sim \sigma n(r^*, T)$, where σ is defined by Eq. (A7) and $n(r^*, T)$ is defined by Eq. (A3). The numerical value for $\lambda(r^*)$ is much greater than λ_D—i.e., $\lambda(r^*) \gg \lambda_D$. Therefore, the effective screening occurs on scales of the order of $\lambda(r^*)$, not λ_D.

Furthermore, the density (A6) of the e^+e^- pairs (which are treated as external charges) is also greater than the background density (A3) at distance r^*. Therefore, we do not expect that the Debye screening is operational in the present circumstances, and we neglect it in our order-of-magnitude estimate [Eq. (A13)].

One should also mention that the density of photons n_γ at this temperature T in this region is much higher than the density of e^+e^- pairs [Eq. (A6)] by at least a factor of $(2\pi\alpha^{-1})\exp(2m/T)$ (see Appendix B in Ref. [85]). These photons with typical frequencies $\omega \sim T$ may leave the system. In fact, they provide the dominant cooling mechanism in the atmosphere, as we already mentioned in the main text. However, we are not interested in the fate of these photons in the present work, as they will be quickly absorbed within relatively short distances from the path of the AQN.

The arguments above conclude numerous suppression factors entering Eq. (A13). This implies a considerable uncertainty in the estimates for the effective number N of the emitted electrons, which are accelerated to 10 MeV energies and leave the system. The emitted electrons can propagate for up to several kilometers, the mean free path in the atmosphere for such energetic electrons. With such uncertainty, we treat N as a parameter constrained by $N \ll N_{\max}$ in the main text. A precise estimate is challenging, as it is a prerogative of the nonequilibrium dynamics, a topic well beyond the scope of the present work.

In our estimates, we assume that most of the electrons will be accelerated from the region $\sim r^*$, because from this region the electrons may get accelerated without much collision with positrons from the electrosphere. However, we generally expect that the accelerated particles cover the entire range of the spectrum, $E \in (1\text{–}10^2)$ MeV, which can leave the system. For qualitative analysis, we assume that the peak of this distribution is on the order of 10 MeV—i.e.,

$$\langle E\rangle \sim U(r^*) \sim 10\ \text{MeV}, \qquad E \in (1-10^2)\ \text{MeV}, \tag{A15}$$

which is precisely the magnitude we used in all our estimates in the main text.

APPENDIX B: PIERRE AUGER CONSTRAINT ON UPWARD-GOING SHOWERS

The constraints on upward-going showers according to the Fluorescence Detector have recently been published in Refs. [96,97]. The upper limits for upward-going showers with energies larger than $E > 10^{17.5}$ eV have been formulated as

$$\begin{aligned} F^{95\%}_{\gamma=1} &= \frac{3.6\times10^{-20}}{\text{cm}^2\cdot\text{s}\cdot\text{sr}} \simeq \frac{1.1\times10^{-2}}{\text{km}^2\cdot\text{yr}\cdot\text{sr}},\\ F^{95\%}_{\gamma=2} &= \frac{8.5\times10^{-20}}{\text{cm}^2\cdot\text{s}\cdot\text{sr}} \simeq \frac{2.6\times10^{-2}}{\text{km}^2\cdot\text{yr}\cdot\text{sr}}, \end{aligned} \tag{B1}$$

where the parameter γ is defined as the spectral index $E^{-\gamma}$ for upward-going showers induced by the primary particle with energy E. We also expressed the upper limits in the same units $\text{km}^{-2}\,\text{yr}^{-1}$ which we used for the AQN flux hitting the Earth, as defined by Eqs. (4) and (6) for comparison.

One can naively think that the upper-limit constraints in Eq. (B1) are already in contradiction with the AQN flux [Eq. (6)], which has been used in our estimates. However, in fact there is no contradiction here, as the upper limit constraints (B1) cannot be directly applied to the AQN upward events. The main point here is that the AQNs are slow-moving nonrelativistic objects with typical velocity $v_{\text{AQN}} \sim 10^{-3}c$, while the conventional analysis assumes that the primary particle is an ultrarelativistic particle moving with the speed of light c. It obviously implies that all bin time detectors are not properly adjusted for such slow-moving AQNs.

Furthermore, the discrimination of the signal from background events is achieved by using the profile constrained geometry fit reconstruction (PCGF) that forces the depth profile to match the approximately universal characteristics of air showers induced by most primaries with a well-defined shower maximum of known width. As we discussed at length in this work, such notions as a “central axis” and a “pancake” do not exist in the AQN framework. Instead, the AQN-induced event should be viewed as a uniform front when the number of particles per unit area does not much depend on the distance from the central axis.[9] It is obvious that this picture of the AQN-induced event is dramatically different from the criteria being used in Ref. [96] to select a proper upward-going air shower reconstructed by PCGF.

Therefore, the upper limits in Eq. (B1) do not impose any constraints on the AQN-induced events. At the same time, the upper limits (B1) strongly constrain the physical models when the shower is initiated by τ leptons being produced from τ neutrinos (or some BSM particle) interacting with the Earth's material [97], because in this scenario the shower is expected to have the conventional universal characteristics such that the PCGF reconstruction properly selects such events.

---

[9] This last feature plays a very important role in our prediction for the radio signal induced by the AQN, as remarked in the Conclusion in item 1.

[1] P. W. Gorham *et al.* (ANITA Collaboration), Phys. Rev. Lett. **117**, 071101 (2016).
[2] P. W. Gorham *et al.* (ANITA Collaboration), Phys. Rev. Lett. **121**, 161102 (2018).
[3] P. W. Gorham *et al.* (ANITA Collaboration), Phys. Rev. Lett. **126**, 071103 (2021).
[4] A. R. Zhitnitsky, J. Cosmol. Astropart. Phys. 10 (2003) 010.
[5] D. B. Fox, S. Sigurdsson, S. Shandera, P. Mészáros, K. Murase, M. Mostafá, and S. Coutu, arXiv:1809.09615.
[6] A. Romero-Wolf *et al.*, Phys. Rev. D **99**, 063011 (2019).
[7] M. G. Aartsen *et al.* (IceCube Collaboration), Astrophys. J. **892**, 53 (2020).
[8] P. Motloch, J. Alvarez-Muñiz, P. Privitera, and E. Zas, Phys. Rev. D **95**, 043004 (2017).
[9] K. D. de Vries and S. Prohira, Phys. Rev. Lett. **123**, 091102 (2019).
[10] P. Dasgupta and P. Jain, Astropart. Phys. **128**, 102530 (2021).
[11] I. M. Shoemaker, A. Kusenko, P. K. Munneke, A. Romero-Wolf, D. M. Schroeder, and M. J. Siegert, Annals of Glaciology **61**, 92 (2020).
[12] D. Smith *et al.*, J. Cosmol. Astropart. Phys. 04 (2021) 016.
[13] B. Chauhan and S. Mohanty, Phys. Rev. D **99**, 095018 (2019).
[14] L. Heurtier, Y. Mambrini, and M. Pierre, Phys. Rev. D **99**, 095014 (2019).
[15] D. Hooper, S. Wegsman, C. Deaconu, and A. Vieregg, Phys. Rev. D **100**, 043019 (2019).
[16] L. A. Anchordoqui *et al.*, Proc. Sci. ICRC2019 (**2020**) 884 [arXiv:1907.06308].
[17] L. A. Anchordoqui, V. Barger, J. G. Learned, D. Marfatia, and T. J. Weiler, Lett. High Energy Phys. **1**, 13 (2018).
[18] E. Dudas, T. Gherghetta, K. Kaneta, Y. Mambrini, and K. A. Olive, Phys. Rev. D **98**, 015030 (2018).
[19] G.-y. Huang, Phys. Rev. D **98**, 043019 (2018).
[20] A. Connolly, P. Allison, and O. Banerjee, arXiv:1807.08892.
[21] J. F. Cherry and I. M. Shoemaker, Phys. Rev. D **99**, 063016 (2019).
[22] L. A. Anchordoqui and I. Antoniadis, Phys. Lett. B **790**, 578 (2019).
[23] J. H. Collins, P. S. Bhupal Dev, and Y. Sui, Phys. Rev. D **99**, 043009 (2019).
[24] L. Heurtier, D. Kim, J.-C. Park, and S. Shin, Phys. Rev. D **100**, 055004 (2019).
[25] S. Chipman, R. Diesing, M. H. Reno, and I. Sarcevic, Phys. Rev. D **100**, 063011 (2019).
[26] M. Abdullah, B. Dutta, S. Ghosh, and T. Li, Phys. Rev. D **100**, 115006 (2019).
[27] D. Borah, A. Dasgupta, U. K. Dey, and G. Tomar, Phys. Rev. D **101**, 075039 (2020).
[28] A. Esmaili and Y. Farzan, J. Cosmol. Astropart. Phys. 12 (2019) 017.
[29] I. Esteban, J. Lopez-Pavon, I. Martinez-Soler, and J. Salvado, Eur. Phys. J. C **80**, 259 (2020).
[30] W. Altmannshofer, P. S. B. Dev, A. Soni, and Y. Sui, Phys. Rev. D **102**, 015031 (2020).
[31] J. M. Cline, C. Gross, and W. Xue, Phys. Rev. D **100**, 015031 (2019).
[32] E. Witten, Phys. Rev. D **30**, 272 (1984).
[33] E. Farhi and R. L. Jaffe, Phys. Rev. D **30**, 2379 (1984).
[34] A. De Rujula and S. L. Glashow, Nature **312**, 734 (1984).
[35] J. Madsen, Lect. Notes Phys. **516**, 162 (1999).
[36] X. Liang and A. Zhitnitsky, Phys. Rev. D **94**, 083502 (2016).
[37] S. Ge, X. Liang, and A. Zhitnitsky, Phys. Rev. D **96**, 063514 (2017).
[38] S. Ge, X. Liang, and A. Zhitnitsky, Phys. Rev. D **97**, 043008 (2018).
[39] S. Ge, K. Lawson, and A. Zhitnitsky, Phys. Rev. D **99**, 116017 (2019).
[40] A. Zhitnitsky, Mod. Phys. Lett. A **36**, 2130017 (2021).
[41] R. D. Peccei and H. R. Quinn, Phys. Rev. D **16**, 1791 (1977).
[42] S. Weinberg, Phys. Rev. Lett. **40**, 223 (1978).
[43] F. Wilczek, Phys. Rev. Lett. **40**, 279 (1978).
[44] J. E. Kim, Phys. Rev. Lett. **43**, 103 (1979).
[45] M. A. Shifman, A. I. Vainshtein, and V. I. Zakharov, Nucl. Phys. **B166**, 493 (1980).
[46] M. Dine, W. Fischler, and M. Srednicki, Phys. Lett. **104B**, 199 (1981).
[47] A. R. Zhitnitsky, Yad. Fiz. **31**, 497 (1980) [Sov. J. Nucl. Phys. **31**, 260 (1980)].
[48] K. Van Bibber and L. J. Rosenberg, Phys. Today **59**, 08, 30 (2006).
[49] S. J. Asztalos, L. J. Rosenberg, K. van Bibber, P. Sikivie, and K. Zioutas, Annu. Rev. Nucl. Part. Sci. **56**, 293 (2006).
[50] P. Sikivie, Lect. Notes Phys. **741**, 19 (2008).
[51] G. G. Raffelt, Lect. Notes Phys. **741**, 51 (2008).
[52] P. Sikivie, Int. J. Mod. Phys. A **25**, 554 (2010).
[53] L. J. Rosenberg, Proc. Natl. Acad. Sci. U.S.A. **112**, 12278 (2015).
[54] D. J. E. Marsh, Phys. Rep. **643**, 1 (2016).
[55] P. W. Graham, I. G. Irastorza, S. K. Lamoreaux, A. Lindner, and K. A. van Bibber, Annu. Rev. Nucl. Part. Sci. **65**, 485 (2015).
[56] I. G. Irastorza and J. Redondo, Prog. Part. Nucl. Phys. **102**, 89 (2018).
[57] E. N. Parker, Astrophys. J. **330**, 474 (1988).
[58] A. Zhitnitsky, J. Cosmol. Astropart. Phys. 10 (2017) 050.
[59] N. Raza, L. van Waerbeke, and A. Zhitnitsky, Phys. Rev. D **98**, 103527 (2018).
[60] S. Ge, M. S. R. Siddiqui, L. Van Waerbeke, and A. Zhitnitsky, Phys. Rev. D **102**, 123021 (2020).
[61] R. C. Henry, J. Murthy, J. Overduin, and J. Tyler, Astrophys. J. **798**, 14 (2014).
[62] M. S. Akshaya, J. Murthy, S. Ravichandran, R. C. Henry, and J. Overduin, Astrophys. J. **858**, 101 (2018).
[63] A. Zhitnitsky, Phys. Lett. B **828**, 137015 (2022).
[64] D. M. Jacobs, G. D. Starkman, and B. W. Lynn, Mon. Not. R. Astron. Soc. **450**, 3418 (2015).
[65] K. Lawson, X. Liang, A. Mead, M. S. R. Siddiqui, L. Van Waerbeke, and A. Zhitnitsky, Phys. Rev. D **100**, 043531 (2019).
[66] P. W. Gorham, Phys. Rev. D **86**, 123005 (2012).
[67] P. W. Gorham and B. J. Rotter, Phys. Rev. D **95**, 103002 (2017).
[68] K. Lawson and A. R. Zhitnitsky, Phys. Rev. D **95**, 063521 (2017).

[69] A. Zhitnitsky, Phys. Rev. D **101**, 083020 (2020).

[70] J. Singh Sidhu, R. J. Scherrer, and G. Starkman, Phys. Lett. B **807**, 135574 (2020).

[71] D. Budker, V. V. Flambaum, and A. Zhitnitsky, Symmetry **14**, 459 (2022).

[72] D. Budker, V. V. Flambaum, X. Liang, and A. Zhitnitsky, Phys. Rev. D **101**, 043012 (2020).

[73] X. Liang, E. Peshkov, L. Van Waerbeke, and A. Zhitnitsky, Phys. Rev. D **103**, 096001 (2021).

[74] N. L. Figueroa, D. Budker, and E. M. Rasel, Quantum Sci. Technol. **6**, 034004 (2021).

[75] R. Abbasi *et al.* (Telescope Array Project Collaboration), Phys. Lett. A **381**, 2565 (2017).

[76] T. Okuda, J. Phys. Conf. Ser. **1181**, 012067 (2019).

[77] P. Abreu *et al.* (Pierre Auger Collaboration), Proc. Sci. ICRC2021 (**2021**) 395.

[78] R. Colalillo, in *European Physical Journal Web of Conferences*, European Physical Journal Web of Conferences, Vol. 197 (EDP Sciences, 2019), p. 03003.

[79] R. Colalillo, Proc. Sci. ICRC2017 (**2017**) 314.

[80] D. Beznosko, R. Beisembaev, K. Baigarin, E. Beisembaeva, O. Dalkarov, V. Ryabov, T. Sadykov, S. Shaulov, A. Stepanov, M. Vildanova, N. Vildanov, and V. Zhukov, in *European Physical Journal Web of Conferences*, European Physical Journal Web of Conferences, Vol. 145 (EDP Sciences, 2017), p. 14001.

[81] D. Beznosko, R. Beisembaev, E. Beisembaeva, O. D. Dalkarov, V. Mossunov, V. Ryabov, S. Shaulov, M. Vildanova, V. Zhukov, K. Baigarin, and T. Sadykov, Proc. Sci. ICRC2019 (**2019**) 195.

[82] A. Zhitnitsky, J. Phys. G **48**, 065201 (2021).

[83] X. Liang and A. Zhitnitsky, Eur. Phys. J. C **82**, 249 (2022).

[84] A. Zhitnitsky, J. Phys. G **49**, 105201 (2022).

[85] A. Zhitnitsky, Universe **7**, 384 (2021).

[86] G. W. Fraser, A. M. Read, S. Sembay, J. A. Carter, and E. Schyns, Mon. Not. R. Astron. Soc. **445**, 2146 (2014).

[87] S. Ge, H. Rachmat, M. S. R. Siddiqui, L. Van Waerbeke, and A. Zhitnitsky, Phys. Dark Universe **36**, 101031 (2022).

[88] M. M. Forbes and A. R. Zhitnitsky, Phys. Rev. D **78**, 083505 (2008).

[89] H. Schoorlemmer *et al.*, Astropart. Phys. **77**, 32 (2016).

[90] X. Liang, A. Mead, M. S. R. Siddiqui, L. Van Waerbeke, and A. Zhitnitsky, Phys. Rev. D **101**, 043512 (2020).

[91] J. D. Jackson, *Classical Electrodynamics*, 3rd ed. (Wiley, New York, NY, 1999).

[92] T. Huege and H. Falcke, Astron. Astrophys. **412**, 19 (2003).

[93] T. Huege and H. Falcke, Astropart. Phys. **24**, 116 (2005).

[94] J. Singh Sidhu, R. M. Abraham, C. Covault, and G. Starkman, J. Cosmol. Astropart. Phys. 02 (2019) 037.

[95] L. A. Anchordoqui *et al.*, Europhys. Lett. **135**, 51001 (2021).

[96] I. A. Caracas *et al.* (Pierre Auger Collaboration), Proc. Sci. ICRC2021 (**2021**) 1145.

[97] P. Abreu *et al.* (Pierre Auger Collaboration), Proc. Sci. ICRC2021 (**2021**) 1140.

[98] V. V. Usov, Phys. Rev. Lett. **80**, 230 (1998).

[99] V. V. Usov, Astrophys. J. Lett. **550**, L179 (2001).

[100] P. Jaikumar, C. Gale, D. Page, and M. Prakash, Phys. Rev. D **70**, 023004 (2004).

[101] T. Harko and K. S. Cheng, Astrophys. J. **622**, 1033 (2005).

[102] J.-F. Caron and A. R. Zhitnitsky, Phys. Rev. D **80**, 123006 (2009).

[103] B. G. Zakharov, J. Exp. Theor. Phys. **112**, 63 (2011).

[104] B. G. Zakharov, Phys. Lett. B **690**, 250 (2010).

[105] M. M. Forbes, K. Lawson, and A. R. Zhitnitsky, Phys. Rev. D **82**, 083510 (2010).

[106] L. D. Landau and E. M. Lifshitz, *Quantum Mechanics, 3rd Edition* (Butterworth-Heinemann, Oxford, 1977).

[107] L. D. Landau and E. M. Lifshitz, *Statistical Physics, Part-1, 3rd Edition* (Butterworth-Heinemann, Oxford, 1977).